SCIENCE CHINA Information Sciences



• RESEARCH PAPER •

December 2025, Vol. 68, Iss. 12, 220307:1–220307:17 https://doi.org/10.1007/s11432-025-4650-4

Special Topic: Terahertz Communications for 6G and Beyond: How Far Are We?

Joint localization and channel estimation for terahertz near-field ISAC UM-MIMO systems

Yanran SUN, Chuang YANG*, Yuheng FAN, Renzhi YUAN & Mugen PENG

School of Information and Communication Engineering, Beijing University of Posts and Telecommunications,
Beijing 100876, China

Received 29 April 2025/Revised 7 September 2025/Accepted 23 October 2025/Published online 18 November 2025

Abstract The integrated sensing and communication (ISAC) in 6G terahertz (THz) ultra-massive multiple-input multiple-output (UM-MIMO) systems faces challenges in near-field scenarios, where spherical wavefronts introduce coupled angle, distance. Existing schemes often address localization and CSI estimation separately, neglecting their interdependence. This paper proposes a joint uplink localization and CSI estimation scheme for hybrid analog-digital THz UM-MIMO systems. First, a coarse angle-of-arrival (AoA) estimation method is developed using DFT-based analog combiners, exploiting near-field angular spread effects. Then, a refined localization scheme iteratively optimizes angle and distance parameters via dynamic interval contraction, reducing computational complexity. Further, a line-of-sight (LoS) -prior-enhanced CSI estimation (LPE-CE) method decouples LoS and non-line-of-sight (NLoS) components using subspace-orthogonal combiners and introduces an adaptive polar-domain codebook that dynamically expands based on residual thresholds. Simulations demonstrate the proposed scheme achieves sub-meter localization accuracy with low complexity, while LPE-CE outperforms benchmarks and adaptively reduces codebook size efficiently.

Keywords terahertz, integrated sensing and communication, near field, localization, channel estimation

Citation Sun Y R, Yang C, Fan Y H, et al. Joint localization and channel estimation for terahertz near-field ISAC UM-MIMO systems. Sci China Inf Sci, 2025, 68(12): 220307, https://doi.org/10.1007/s11432-025-4650-4

1 Introduction

With the rapid development of wireless communication technology, the research on the sixth generation (6G) mobile communication system has become a hot topic in both academic and industrial communities [1]. The 6G era is expected to bring unprecedented data rates, connection density, and communication experience, while also promoting the deep integration of sensing and communication technologies. Integrated sensing and communication (ISAC), as one of the important features of 6G, aims to achieve seamless integration of communication systems and perception systems, thereby improving spectrum utilization efficiency, reducing hardware costs, and opening up new application scenarios such as intelligent transportation, environmental monitoring, and augmented reality [2,3].

To achieve efficient collaboration of ISAC, wider bandwidth and large-scale antenna arrays become inevitable requirements. The terahertz (THz) band, with its rich spectrum resources and ultra-high data transmission capabilities, emerges as a potential frequency band for 6G communications [4,5]. Ultra-massive multiple-input multiple-output (UM-MIMO) technology, which leverages hundreds to thousands of antenna elements, offers significant array gain to overcome the high path loss of THz, positioning it as a key technology to support 6G THz high-capacity, low-latency communication [6].

In THz ISAC UM-MIMO systems, location information and channel state information (CSI) are two critical parameters [7]. Location information supports user positioning and tracking, while also facilitating beamforming and resource allocation by providing spatial awareness of the environment [8]. Meanwhile, CSI is the basis for efficient data transmission and interference management [9]. Consequently, precise estimation of location and CSI is crucial for the performance of ISAC systems and has become a research hotspot.

^{*} Corresponding author (email: chuangyang@bupt.edu.cn)

1.1 Related work

Early research on joint location and CSI estimation predominantly focused on full-digital architectures. Ref. [10] proposed a two-stage joint target detection and channel estimation (CE) scheme, exploiting the joint burst sparsity of sensing and communication channel to enhance detection and estimation performance. In [11], an uplink sensing-aided Kalman-filter-based CE scheme was proposed, which exploited the angle-of-arrival (AoA) estimated by the multiple signal classification (MUSIC) method to improve the CSI estimation accuracy. A simultaneous weighting orthogonal matching pursuit-sparse Bayesian learning scheme was proposed in [12], which efficiently estimated the AoA information and incorporated it in the CE procedure. In [13], a sensing-assisted sparse channel recovery scheme for UM-MIMO systems was proposed, where the scatterer location was sensed by the echo pilot signal, and the sparse channel was estimated by the compressive sensing (CS) method exploiting the sensing location information. However, these schemes require direct access to signals from each antenna element, resulting in high hardware complexity and power consumption [14]. In UM-MIMO systems, such full-digital architectures become impractical due to cost and scalability constraints, prompting a shift toward hybrid architectures to address these limitations.

To mitigate the challenges of full-digital systems, hybrid analog and digital architectures have been proposed, reducing the number of radio frequency (RF) chains to balance performance and cost [15, 16]. And within hybrid architectures, several research studies on location and CSI estimation have emerged. In terms of location sensing, based on the far-field assumption, research mainly focused on AoA estimation by designing analog and digital combiners [17–19]. Ref. [17] proposed a dynamic maximum likelihood estimator suitable for hybrid architectures, and derived the closed-form expression of cramer-rao bound (CRB) to evaluate the achievable AoA estimation performance. By switching the analog combiners to a set of predefined angles to reconstruct the signal covariance matrix, in [18], AoAs of the signal were estimated by applying the MUSIC algorithm. Ref. [19] designed a set of analog combiners that collectively span the entire space, and then performed an exhaustive search over the analog and digital combiners to estimate AoA. As for CSI estimation, the CS method has been widely used due to its ability to efficiently process compressed high-dimensional sparse channels. Ref. [20] proposed two compressive hybrid MIMO CE schemes to recover the channel matrix by exploiting the spatially sparse structure in the far-field MIMO channel.

However, with the growing scale of UM-MIMO antenna arrays, the wavefront emitted by a source within a certain range becomes spherical when it reaches the array, and the near-field effects have become significant [21]. Unlike the far-field planar wavefront, such a spherical wavefront brings another degree of freedom to the channel in addition to AoA: distance. Hence, existing research turns to both near-field localization and CE in hybrid architectures. In [22], an efficient near-field localization scheme for hybrid analog and digital UM-MIMO systems was proposed, which reduced the high computational complexity by the design of the analog and digital combiner decoupling AoA and distance estimation. Ref. [23] proposed a polar-domain representation that makes the near-field channel exhibit sparsity, and achieved an accurate near-field sparse CE by the CS method. Based on this, Ref. [24] proposed a two-dimensional polar-angular-domain sparse representation for THz widely-spaced multi-subarray systems. These studies typically address localization and CE independently, failing to account for the intrinsic coupling between AoA, distance and CSI in near-field scenarios. This lack of integration limits their applicability in ISAC systems, where joint estimation is critical for optimal performance.

Recent efforts have explored joint localization and CE in near-field hybrid architectures. In [25], a sensing-enhanced uplink CE scheme for near-field UM-MIMO systems based on a novel transceiver architecture was proposed. This architecture comprises a sensing module for power sensing and a training module for baseband processing, relying on RF switches adopted on antenna elements to keep the two modules switching. While the approach shows promising results in lower-frequency bands, it increases system complexity and cost, limiting practical deployment. More critically, this scheme is unsuitable for THz bands, where the symbol duration reaches on the order of nanoseconds. As the baseband ADC stabilization time is on the order of milliseconds [26], leading to the loss of a large number of symbols during switches between two modules, which disrupts real-time data transmission and degrades spectral efficiency.

1.2 Contributions

In contrast to prior work, in this paper, we propose a novel joint uplink localization and CE scheme for THz near-field UM-MIMO systems in hybrid analog and digital architectures, eliminating the reliance on additional sensing devices. Our contributions are summarized as follows.

- Inspired by the far-field AoA estimation scheme [17, 19], we reveal the near-field spatial angular spread effect, and then propose a coarse line-of-sight (LoS) angle estimation scheme by DFT-based analog combiners.
- We propose a refined user localization scheme based on joint parameter optimization, which iteratively refines angle and estimates distance parameters by leveraging the high-degree-of-freedom characteristics in the digital domain. During the alternating optimization of angle and distance parameters, we employ the dynamic interval contraction to progressively reduce the search space, thereby converging to the optimal solution, lowering computational complexity, and avoiding local optima.
- Exploiting the estimated user location, we propose a LoS-prior-enhanced CE (LPE-CE) scheme which strategically decouples the LoS and non-line-of-sight (NLoS) components through subspace-orthogonal analog combiners, and estimates the channel components separately to avoid NLoS components being masked. Additionally, we introduce an adaptive near-field polar-domain codebook based on LoS prior, which initializes with a minimal set of distance rings and iteratively expands based on residual thresholds, achieving lower average complexity compared to the conventional polar-domain codebook [23].
- Simulation results demonstrate that the proposed localization scheme achieves accurate localization with less computational complexity. Additionally, the proposed LPE-CE scheme achieves superior estimation performance while employing an adaptive codebook design that efficiently reduces the average codebook size compared to the conventional codebook.

The rest of this paper is organized as follows. In Section 2, the transmission protocol, signal model, and THz near-field channel model are introduced. Section 3 introduces the near-field localization scheme, and the LoS-prior-enhanced CE scheme is proposed in Section 4. The simulation results are then presented in Section 5. Finally, the conclusion is drawn in Section 6.

1.3 Notations

Notations used in this paper are explained as follows. Lower-case and upper-case boldface letters represent vectors and matrices, respectively; $(\cdot)^{\mathrm{T}}$, $(\cdot)^{\mathrm{H}}$, $(\cdot)^{-1}$, $(\cdot)^{\dagger}$ denote the transpose, conjugate transpose, inverse, and pseudo inverse of matrix \mathbf{A} , respectively; $\mathbf{a}[i]$ and $\mathbf{A}[i,j]$ denote the *i*-th elements of \mathbf{a} vector and the (i,j)-th entry of the matrix \mathbf{A} , respectively; $\mathbf{B} = \mathrm{blkdiag}(\mathbf{A}_1, \mathbf{A}_2, \dots, \mathbf{A}_n)$ returns a block diagonal matrix by aligning $\mathbf{A}_1, \mathbf{A}_2, \dots, \mathbf{A}_n$ along the diagonal. $\mathcal{CN}(\mu, \sigma^2)$ is a complex normal distribution with mean μ and covariance σ^2 .

2 System model

As shown in Figure 1, we consider an uplink time division duplexing (TDD) based multi-user THz UM-MIMO system. The base station (BS) is equipped with a uniform linear array (ULA) with N antennas to simultaneously serve P single-antenna users randomly distributed over the cell. The fully connected hybrid analog and digital architecture with M RF chains is employed at the BS. For uplink transmission, we assume the users transmit mutually orthogonal pilot sequences to the BS, thus, the localization and CE are independent for each of them. Without loss of generality, we consider an arbitrary user for analysis.

2.1 Transmission protocol and signal model

In this paper, we propose that sensing and wireless communication are implemented in one system and exploit the sensing location knowledge to enhance CE. To this end, our proposed scheme is based on a specific transmission protocol, as described in Figure 2. Specifically, there are T transmission slots in the considered time interval, and the channel remains unchanged within such channel coherence time. During the pilot transmission phase, the protocol comprises two sequential stages: (i) angle-distance sensing via Q_1 -slot uplink transmission of sensing pilots from the user to the BS; (ii) CE through Q_2 -slot CE pilots leveraging acquired location parameters for adaptive codebook optimization. Finally, in the remaining $T - Q_1 - Q_2$ slots, uplink data transmission is carried out between the BS and the user.

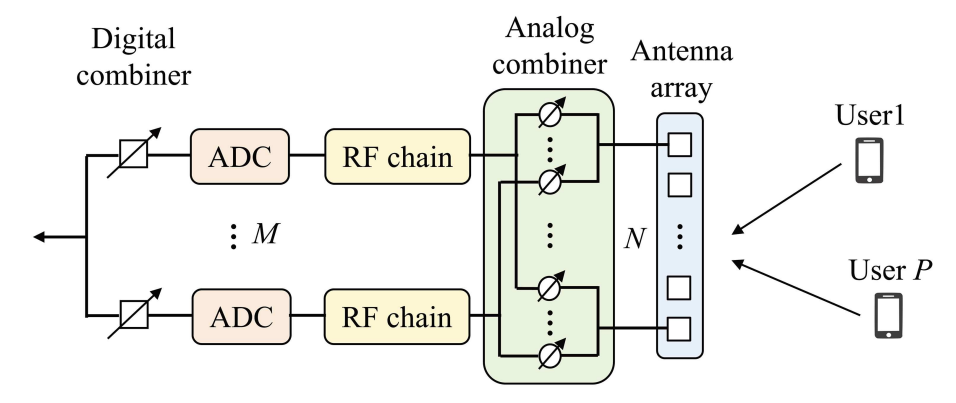
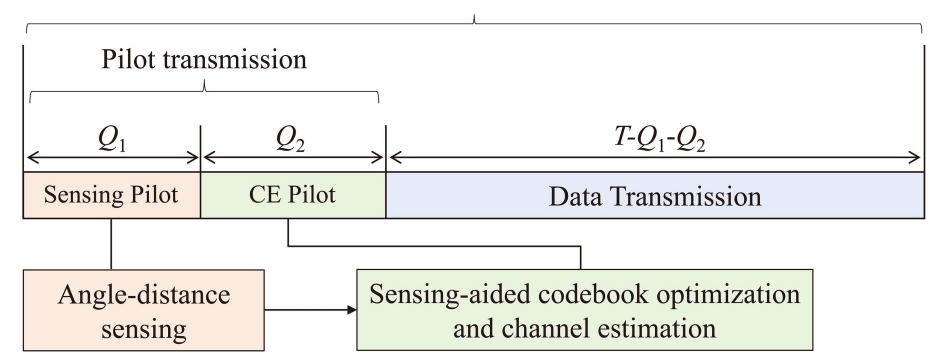


Figure 1 (Color online) THz UM-MIMO system with hybrid analog and digital architecture.

T transmission slots



 ${\bf Figure~2} \quad \hbox{(Color online) Transmission protocol of proposed scheme}.$

For ease of presentation, we use Q to uniformly denote the pilot length of sensing and CE in the pilot transmission phase. Let s_q denote the transmit pilot in the time slot q. By assuming that $s_q = 1$ for all $q = 1, \ldots, Q$, the received signal vector $\mathbf{y}_q \in \mathbb{C}^{M \times 1}$ can be represented as

$$\mathbf{y}_{q} = \mathbf{V}_{A,q}^{\mathrm{H}} \mathbf{h} s_{q} + \mathbf{V}_{A,q}^{\mathrm{H}} \mathbf{w}_{q} = \mathbf{V}_{A,q}^{\mathrm{H}} \mathbf{h} + \mathbf{V}_{A,q}^{\mathrm{H}} \mathbf{w}_{q}, \tag{1}$$

where $\mathbf{V}_{A,q} \in \mathbb{C}^{N \times M}$ is the analog combiner matrix in the q-th slot, satisfying the constant modulus constraint $|\mathbf{V}_{A,q}(i,j)| = \frac{1}{\sqrt{N}}$. $\mathbf{h} \in \mathbb{C}^{N \times 1}$ denotes the channel vector, and $\mathbf{w}_q \sim \mathcal{CN}(0,\sigma^2)$ denotes the additive Gaussian noise. Via digital combiner operation, the baseband received signal

$$x_q = \mathbf{v}_{D,q}^{\mathrm{H}} \mathbf{V}_{A,q}^{\mathrm{H}} \mathbf{h} + \mathbf{v}_{D,q}^{\mathrm{H}} \mathbf{V}_{A,q}^{\mathrm{H}} \mathbf{w}_q, \tag{2}$$

where $\mathbf{v}_{D,q} \in \mathbb{C}^{M \times 1}$ is the digital combiner vector in the q-th slot.

2.2 THz near-field channel model

The THz near-field signal transmitted by each user propagates through a multipath channel with L+1 distinct paths and is captured by the N receiving antennas, where there is one LoS path and the remaining L scatters are randomly distributed in the near-field region. Due to the high susceptibility to blockage, reflection, and scattering, NLoS paths in THz channels experience severe attenuation, making the LoS path dominant and accounting for the majority of the received energy, particularly at short ranges [27], with the power ratio of the LoS path to the total NLoS paths typically ranging from 10 to 20 dB [28,29]. Therefore, the THz near-field channel can be characterized as [30]

$$\mathbf{h} = \mathbf{h}_{\text{LoS}} + \mathbf{h}_{\text{NLoS}} = \alpha_0 \mathbf{b}(\theta_0, r_0) + \sum_{l=1}^{L} \alpha_l \mathbf{b}(\theta_l, r_l), \tag{3}$$

where l = 0 denotes the LoS path. α_l, r_l , and $\theta_l = \sin \phi_l$ represent the complex path gain, the distance, and the spatial angle of the l-th path, respectively. As the LoS path dominant, there have $|\alpha_0| \gg |\alpha_l|$ $(l \neq 0)$.

 ϕ_l is the AoA of the l-th path. And $\mathbf{b}(\theta, r)$ is the near-field steering vector given as [23]

$$\mathbf{b}(\theta, r) = \left[e^{-j\frac{2\pi}{\lambda}\Delta r^{(1)}}, e^{-j\frac{2\pi}{\lambda}\Delta r^{(2)}}, \dots, e^{-j\frac{2\pi}{\lambda}\Delta r^{(N)}} \right]^{\mathrm{T}}, \tag{4}$$

where λ represents the carrier wavelength, $\Delta r^{(n)} = r^{(n)} - r$, $r^{(n)}$ is the distance between the *n*-th BS antenna and the user that can be derived as $r^{(n)} = \sqrt{r^2 + p_n^2 d^2 - 2r p_n d\theta}$ with $\theta \in [-1,1]$. $p_n = n - \frac{N-1}{2}, n = 1, 2, \ldots, N$ is the antenna location. The antenna spacing d is set to half-wavelength as $d = \frac{\lambda}{2}$ [31].

3 Localization scheme

In this section, we propose a near-field localization scheme for hybrid analog and digital architectures. Firstly, we propose a coarse LoS angle estimation scheme based on DFT-based analog combiners by revealing the near-field spatial angular spread effect. Then, we propose a refined user localization scheme based on joint parameter optimization, which iteratively refines angle and estimates distance parameters by leveraging the high-degree-of-freedom characteristics in the digital domain.

3.1 Coarse angle estimation by DFT-based analog combiners

In the hybrid analog and digital architecture, the received signal is first processed by the analog combiner matrix \mathbf{V}_A , as (1) shows. Existing far-field AoA estimation schemes typically use the DFT matrix $\mathbf{F} = \frac{1}{\sqrt{N}}[\mathbf{a}(\bar{\theta}_0),\ldots,\mathbf{a}(\bar{\theta}_{N-1})]$ as the analog combiner matrix, as each of its columns $\mathbf{a}(\bar{\theta}_n) = [\mathrm{e}^{\mathrm{j}\pi\bar{\theta}_1},\ldots,\mathrm{e}^{\mathrm{j}\pi\bar{\theta}_N}]^\mathrm{T}$ corresponds to a specific angular sector in the spatial domain, where $\bar{\theta}_n = n - \frac{N-1}{2}$. Signals with AoA outside of the given sector are attenuated or even nullified, enabling the system to quickly identify the angle of the received signal [19]. But for the near-field signal, the additional distance dimension causes the energy spread effect in the spatial angular domain, resulting in reduced accuracy of the sector angle response [23]. In this subsection, we specifically analyze the near-filed energy spread effect in the spatial angular domain. Based on this, we perform a coarse angle estimation by DFT-based analog combiners.

3.1.1 Analysis of near-field spatial angular spread effect

In order to determine the near-field spatial angular spread effect, we first derive the m-th entry of the analog received signal \mathbf{y}_q in (1) as

$$\mathbf{y}_{q}[m] = \mathbf{v}_{A,q,m}^{\mathrm{H}} \mathbf{h} + \mathbf{v}_{A,q,m}^{\mathrm{H}} \mathbf{w}_{q}$$

$$= \sum_{l=0}^{L} \alpha_{l} \mathbf{v}_{A,q,m}^{\mathrm{H}} \mathbf{b}(\theta_{l}, r_{l}) + \mathbf{v}_{A,q,m}^{\mathrm{H}} \mathbf{w}_{q},$$
(5)

where $\mathbf{v}_{A,q,m}$ is the m-th column of the combiner matrix $\mathbf{V}_{A,q}$. Let $\mathbf{v}_{A,q,m} = \mathbf{a}(\bar{\theta}_n)$, we have

$$\mathbf{y}_{q}[m] = \sum_{l=0}^{L} \alpha_{l} \mathbf{a}^{H}(\bar{\theta}_{n}) \mathbf{b}(\theta_{l}, r_{l}) + \mathbf{v}_{A,q,m}^{H} \mathbf{w}_{q}.$$

$$(6)$$

And the near-field spatial angular spread effect is determined by $\mathbf{a}^{\mathrm{H}}(\bar{\theta}_n)\mathbf{b}(\theta_l, r_l)$ [23]. Thus, we define the amplitude function of $\mathbf{a}^{\mathrm{H}}(\bar{\theta}_n)\mathbf{b}(\theta_l, r_l)$ as follows:

$$\Upsilon\left(\bar{\theta}_{n}, \theta_{l}, r_{l}\right) = \left|\mathbf{a}^{H}\left(\bar{\theta}_{n}\right) \mathbf{b}\left(\theta_{l}, r_{l}\right)\right| \\
\stackrel{(a)}{\approx} \frac{1}{N} \left|\sum_{n=1}^{N} \exp\left(j\frac{2\pi}{\lambda}\left(p_{n}d\bar{\theta}_{n} - p_{n}d\theta_{l} + \frac{p_{n}^{2}d^{2}(1 - \theta_{l}^{2})}{2r_{l}}\right)\right)\right| \\
= \frac{1}{N} \left|\sum_{n=1}^{N} \exp\left(j\pi\left(p_{n}\left(\bar{\theta}_{n} - \theta_{l}\right) + p_{n}^{2}\frac{d(1 - \theta_{l}^{2})}{2r_{l}}\right)\right)\right|, \tag{7}$$

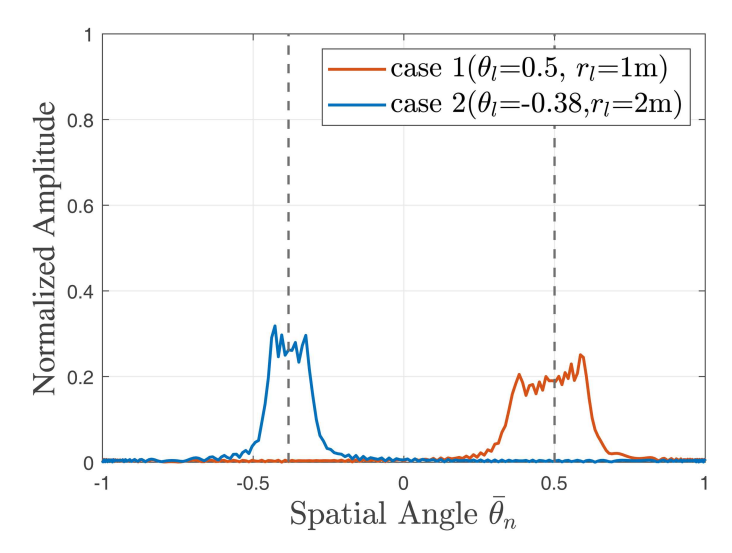


Figure 3 (Color online) Normalized amplitude of $\Upsilon(\bar{\theta}_n, \theta_l, r_l)$ versus $\bar{\theta}_n$ in two cases (the spatial angle θ_l of each case marked by black deshed lines), where N=256 and f=100 GHz.

where (a) is derived by Taylor series to approximate $\Delta r^{(n)} = \sqrt{r^2 + p_n^2 d^2 - 2rp_n d\theta} - r \approx -p_n d\theta + \frac{p_n^2 d^2 (1-\theta^2)}{2r}$. Figure 3 shows the normalized amplitude of $\Upsilon(\bar{\theta}_n, \theta_l, r_l)$ versus $\bar{\theta}_n$. It can be seen that the energy of one near-field path component spreads towards multiple angles around its true spatial angle θ_l . Define the spatial angle range of energy spread:

$$\Theta_{l} = \left\{ \bar{\theta}_{n} | \Upsilon\left(\bar{\theta}_{n}, \theta_{l}, r_{l}\right) > \eta \max_{\bar{\theta}_{n}} \Upsilon\left(\bar{\theta}_{n}, \theta_{l}, r_{l}\right) \right\}, \tag{8}$$

where $\eta \in (0,1)$ is a threshold. And then, we have Theorem 1.

Theorem 1. The true spatial angle θ_l lies approximately at the midrange of Θ_l , i.e.,

$$\theta_l \approx \text{median}(\Theta_l).$$
 (9)

A similar conclusion was also drawn in [32, Observation 1], but no detailed proof was provided therein. Proof. Let $x = p_n \in [-1, 1]$, when $N \to \infty$, Eq. (7) can be approximated as

$$\Upsilon\left(\bar{\theta}_{n}, \theta_{l}, r_{l}\right) \approx \frac{1}{2} \left| \int_{-1}^{1} \exp\left(-j\pi \left(\frac{N^{2}d\left(1 - \theta_{l}^{2}\right)}{8r_{l}}x^{2} - \frac{N\left(\bar{\theta}_{n} - \theta_{l}\right)}{2}x\right)\right) dx \right|
= \frac{1}{2} \left| \int_{-1}^{1} \exp\left(-j\pi \left(G_{1}x - G_{2}\right)^{2}\right) dx \right|,$$
(10)

where $G_1 = \sqrt{\frac{N^2 d(1-\theta_l^2)}{8r_l}}$, $G_2 = \sqrt{\frac{r_l}{2d(1-\theta_l^2)}} (\bar{\theta}_n - \theta_l)$. Then, let $t = \sqrt{2}(G_1x - G_2)^2$, there derives

$$\Upsilon\left(\bar{\theta}_{n}, \theta_{l}, r_{l}\right) = \frac{1}{2\sqrt{2}G_{1}} \left| \int_{-\sqrt{2}(G_{1} - G_{2})}^{\sqrt{2}(G_{1} - G_{2})} \exp\left(-j\frac{\pi}{2}t^{2}\right) dt \right|
= \frac{1}{2\sqrt{2}G_{1}} \left| \left[C\left(\sqrt{2}\left(G_{1} - G_{2}\right)\right) - jS\left(\sqrt{2}\left(G_{1} - G_{2}\right)\right) \right] - \left[C\left(\sqrt{2}\left(G_{1} + G_{2}\right)\right) - jS\left(\sqrt{2}\left(G_{1} + G_{2}\right)\right) \right] \right|
= \frac{1}{2\sqrt{2}G_{1}} \left| \left[C\left(\sqrt{2}\left(G_{1} - G_{2}\right)\right) - C\left(\sqrt{2}\left(G_{1} + G_{2}\right)\right) \right] - j\left[S\left(\sqrt{2}\left(G_{1} - G_{2}\right)\right) - S\left(\sqrt{2}\left(G_{1} + G_{2}\right)\right) \right] \right|,$$
(11)

where $C(\beta) = \int_0^\beta \cos(\frac{\pi}{2}t^2) dt$, $S(\beta) = \int_0^\beta \sin(\frac{\pi}{2}t^2) dt$ are Fresnel functions [33]. For a specific path, the value of G_1 is constant, and the value of G_2 only varies with $\bar{\theta}_n$. Combined with the properties of Fresnel functions, it can be easily derived that $\Upsilon(-G_2) = \Upsilon(G_2) = \Upsilon(|\theta_l - \bar{\theta}_0|)$. Thus, we have $\theta_l \approx \text{median}(\Theta_l)$.

3.1.2 Analog combiners design and coarse angle estimation

Based on Theorem 1, we next design the DFT-based combiner and then perform the coarse angle estimation.

Due to the limited number of RF chains of the hybrid architecture, $\mathbf{V}_{A,q} \in \mathbb{C}^{N \times M}$ cannot directly cover all N spatial angular sectors in the DFT matrix. Therefore, we design a set of analog combiners $\{\mathbf{V}_{A,q}\}_{q=1}^{Q_1}$ in the first Q_1 transmission slots as

$$\mathbf{V}_{A,q} = \left[\mathbf{v}_{A,q,1}, \dots, \mathbf{v}_{A,q,M}\right] = \left[\mathbf{a} \left(\bar{\theta}_{(q-1)M+1}\right), \dots, \mathbf{a} \left(\bar{\theta}_{qM}\right)\right]. \tag{12}$$

Accordingly, let the m-th RF chain analog received signal in the q-th slot $\mathbf{y}_q[m]$ in (5) be denoted as $y(n) = \mathbf{a}^{\mathrm{H}}(\bar{\theta}_n)\mathbf{h} + \mathbf{a}^{\mathrm{H}}(\bar{\theta}_n)\mathbf{w}_q$, where n = (q-1)M + m. Next, to identify signal components likely associated with the dominant LoS path, we introduce a candidate index set \mathcal{N} , defined as

$$\mathcal{N} = \left\{ n \left| |y(n)|^2 > \bar{\eta} \left| \max_n y(n) \right|^2 \right\}, \tag{13}$$

where $\bar{\eta} \in (0,1)$ is the predefined power threshold parameter. This set includes indexes of signals whose power exceeds a fraction $\bar{\eta}$ of the maximum signal power.

Due to the LoS path dominance and accounting for the majority of the received energy in THz near-field channel, it allows us to associate the strongest signal components with the LoS path. By appropriately selecting the value of $\bar{\eta}$, the candidate set \mathcal{N} can effectively capture the spatial angle range index corresponding to the energy distribution of the LoS path. Finally, the spatial angle of the LoS path can be estimated as $\hat{\theta}_0^C = \bar{\theta}_{\text{median}(\mathcal{N})}$ by Theorem 1.

3.2 Refined angle and distance estimation by joint parameter optimization

Having completed the design of analog combiners in the above subsection, we obtain the candidate index set \mathcal{N} , which indicates a preliminary angle estimation of the LoS path, i.e., $\hat{\theta}_0^C = \bar{\theta}_{\mathrm{median}(\mathcal{N})}$. To further refine the angle estimation and additionally estimate the distance of the LoS path, in this subsection, we next propose a refined LoS path estimation method based on joint parameter optimization, iteratively refining angle and estimating distance parameters by leveraging the high-degree-of-freedom characteristics in the digital domain.

Firstly, define $\mathcal{Q} = \left\{ \left\lfloor \frac{n-1}{M} \right\rfloor + 1 | n \in \mathcal{N} \right\}$ as the set of candidate time slots corresponding to all analog combiner vectors associated with $\mathcal{N}, \ |\mathcal{Q}| = I$. Then, we have the corresponding analog output $\mathbf{y}_{\bar{q}} = \mathbf{V}_{A,\bar{q}}^{\mathrm{H}} + \mathbf{V}_{A,\bar{q}}^{\mathrm{H}} \mathbf{w}_{\bar{q}}$, where $\mathbf{V}_{A,\bar{q}}$ is the analog combiner in the \bar{q} -th slot, $\bar{q} \in \mathcal{Q}$. This way, an exhaustive search by excluding spatial sectors can be avoided. Let the optimal digital combiner corresponding to $\mathbf{V}_{A,\bar{q}}$ be $\mathbf{v}_{D,\bar{q}}$. Stacking all $\bar{q} \in \mathcal{Q}$ slots, the analog output and optimal digital combiner can be denoted as $\bar{\mathbf{y}} = \mathrm{diag}(\mathbf{y}_{\bar{q}_1}, \dots, \mathbf{y}_{\bar{q}_I}) \in \mathbb{C}^{IM \times I}$, and $\bar{\mathbf{v}}_D = [\mathbf{v}_{D,\bar{q}_1}^{\mathrm{T}}, \dots, \mathbf{v}_{D,\bar{q}_I}^{\mathrm{T}}]^{\mathrm{T}} \in \mathbb{C}^{IM \times 1}$, respectively. The baseband received signal thereby is $\bar{\mathbf{x}} = \bar{\mathbf{v}}_D^{\mathrm{H}} \bar{\mathbf{y}} \in \mathbb{C}^{1 \times I}$.

Theorem 2. Let the whole hybrid combining weight align with the array steering vector, i.e., $\mathbf{V}_{A,q}\mathbf{v}_{D,q} = \mathbf{b}(\theta,r), \theta \in (-1,1)$. For the LoS-dominant THz near-field channel, the baseband received signal power gets maximum when $(\theta,r) = (\theta_0,r_0)$, i.e., $\mathbf{V}_{A,q}\mathbf{v}_{D,q} = \mathbf{b}(\theta_0,r_0)$.

Proof. The received baseband output power from (2) is

$$P_x = \left| (\mathbf{V}_{A,q} \mathbf{v}_{D,q})^{\mathrm{H}} \mathbf{h} \right|^2 + \sigma^2.$$
 (14)

Since the noise power σ^2 is constant, maximizing P_x reduces to maximizing the signal power term $|(\mathbf{V}_{A,q}\mathbf{v}_{D,q})^{\mathrm{H}}\mathbf{h}|^2$. Let $\mathbf{V}_{A,q}\mathbf{v}_{D,q} = \mathbf{b}(\theta,r), \ \theta \in (-1,1),$ there derives

$$\left| \left(\mathbf{V}_{A,q} \mathbf{v}_{D,q} \right)^{\mathrm{H}} \mathbf{h} \right| = \left| \mathbf{b}^{\mathrm{H}}(\theta, r) \mathbf{h} \right| = \left| \sum_{l=0}^{L} \alpha_{l} \mathbf{b}^{\mathrm{H}}(\theta, r) \mathbf{b}(\theta_{l}, r_{l}) \right|. \tag{15}$$

In the LoS-dominant channel, the inner product is dominated by the LoS path's contribution. For arbitrary (θ, r) , apply the triangle inequality:

$$\left|\mathbf{b}^{H}(\theta, r)\mathbf{h}\right| \leqslant \sum_{l=0}^{L} \left|\alpha_{l}\right| \left|\mathbf{b}^{H}(\theta, r)\mathbf{b}(\theta_{l}, r_{l})\right| \leqslant \sum_{l=0}^{L} |\alpha_{l}|, \tag{16}$$

where the upper bound is approached when $(\theta, r) = (\theta_0, r_0)$, as the LoS term $|\alpha_0|$ is maximized while cross terms are minimized. For other (θ, r) , the inner product is reduced due to smaller gains $|\alpha_l|(l \neq 0)$.

Hence, based on Theorem 2, the angle and distance of the LoS path can be estimated by maximizing the following objective function:

$$\left(\hat{\theta}_0, \hat{r}_0\right) = \arg\max_{\theta, r \in \Omega} \|\bar{\mathbf{x}}\|^2, \quad \text{s.t. } \mathbf{V}_{A,\bar{q}} \mathbf{v}_{D,\bar{q}} = \mathbf{b}(\theta, r), \tag{17}$$

where the parameter space $\Omega = (\theta_{\min}, \theta_{\max}) \times (r_{\min}, r_{\max})$. In the constraint, we have $\mathbf{v}_{D,\bar{q}} = \mathbf{V}_{A,\bar{q}}^{\dagger} \mathbf{b}(\theta, r)$, where $\mathbf{V}_{A,\bar{q}}^{\dagger}$ is the left pseudo inverse of $\mathbf{V}_{A,\bar{q}}$. For the given $\mathbf{V}_{A,\bar{q}}$ in the above subsection, as the columns of $\mathbf{V}_{A,\bar{q}}$ are orthogonal, it follows that $\mathbf{v}_D = \mathbf{V}_{A,\bar{q}}^{\dagger} \mathbf{b}(\theta, r) = \frac{1}{N} \mathbf{V}_A^{\mathrm{H}} \mathbf{b}(\theta, r)$.

Next, to solve binary optimization problems efficiently, we propose an alternate optimization scheme, dynamically adjusting the confidence intervals of the parameters to converge toward the globally optimal (θ, r) . This approach significantly reduces the computational complexity of directly optimizing (θ, r) while lowering the risk of conventional gradient-based methods converging to local optima.

- (1) Initially, the confidence interval of θ is set to i.e., $\Psi_{\theta}^{(0)} = [\theta_{\min}^{(0)}, \theta_{\max}^{(0)}] = [\hat{\theta}_{0}^{C} \Delta \theta, \hat{\theta}_{0}^{C} + \Delta \theta]$, where $\Delta \theta$ is a predefined angle spread range. And the confidence interval of r is set to its full domain, i.e., $\Psi_{r}^{(0)} = [r_{\min}^{(0)}, r_{\max}^{(0)}]$. At each iteration t, the algorithm cyclically optimizes one parameter while fixing another to the midpoint of its current intervals.
- (2) A uniform sampling operator $\mathcal{S}(\Psi^{(t)},K) = \{\Psi_{\min} + \frac{i-1}{K-1}(\Psi_{\max} \Psi_{\min})\}_{i=1}^K$ generates K equidistant points within $\Psi^{(t)}$, and the objective function is evaluated at these points. The top $\lceil \tau K \rceil$ ($\tau \in (0,0.5]$) samples with the highest function values are retained, and the updated interval $\Psi^{(t+1)}$ is defined as the minimum and maximum of these selected points, ensuring $\Psi^{(t+1)} \subseteq \Psi^{(t)}$. The process alternates across both parameters until their intervals converge to a specified tolerance ϵ , i.e., $\Psi^{(t)} < \epsilon$.

3.3 Proposed localization algorithm

The overall localization procedure is summarized in Algorithm 1.

```
Algorithm 1 Proposed localization algorithm.
```

```
Input: Received signal \{\mathbf{y}_q\}_{q=1}^{Q_1}, predefined threshold \bar{\eta}, tolerance error \epsilon, sampling number K, interval shrinkage ratio \tau.
Output: Estimated localization (\hat{\theta}_0, \hat{r}_0).
 1: Stage 1: coarse angle estimation
 2: for q = 1, ..., Q_1 do
         Apply V_{A,q} in (12) to acquire y(n);
 4: end for
 5: Calculate \mathcal{N} = \{ n ||y(n)|^2 > \bar{\eta} |\max_n y(n)|^2 \} in (13);
 6: \hat{\theta}_0^C = \bar{\theta}_{\text{median}(N)};
7: Stage 2: refined angle and distance estimation
 8: Calculate Q = \left\{ \left| \frac{n-1}{M} \right| + 1 | n \in \mathcal{N} \right\} \text{ and } \bar{\mathbf{y}};
 9: Initialize confidence interval \Psi_{\theta}^{(0)} = \left[\hat{\theta}_0^C - \Delta\theta, \hat{\theta}_0^C + \Delta\theta\right], \Psi_r^{(0)} = \left[r_{\min}^{(0)}, r_{\max}^{(0)}\right]
            \theta \leftarrow \mathbb{E}[\varPsi_{\theta}^{(t)}] \text{, generate samples of } r \text{: } \mathcal{S}_r^{(t)} = \mathcal{S}(\varPsi_r^{(t)}, K);
11:
            Compute the value of the objective function f in (17), and generate \mathcal{F}_r^{(t)} = \{f(\theta,r) | r \in \mathcal{S}_r^{(t)}\};
12:
            Interval contraction: \Psi_r^{(t+1)} \leftarrow \left[ \min \left( \mathcal{S}_r^{(t)}[\mathcal{I}_r^{(t)}] \right), \max \left( \mathcal{S}_r^{(t)}[\mathcal{I}_r^{(t)}] \right) \right], where \mathcal{I}_r^{(t)} is the index set of the top \lceil \tau K \rceil highest
13:
            r \leftarrow \mathbb{E}[\Psi_r^{(t+1)}], generate samples of \theta: \mathcal{S}_{\theta}^{(t)} = \mathcal{S}(\Psi_{\theta}^{(t)}, K);
            Compute the value of the objective function f in (17), and generate \mathcal{F}_{\theta}^{(t)} = \{f(\theta, r) | \theta \in \mathcal{S}_{\theta}^{(t)}\};
15:
            Interval contraction: \Psi_{\theta}^{(t+1)} \leftarrow \left[\min\left(\mathcal{S}_{\theta}^{(t)}[\mathcal{I}_{\theta}^{(t)}]\right), \max\left(\mathcal{S}_{\theta}^{(t)}[\mathcal{I}_{\theta}^{(t)}]\right)\right], where \mathcal{I}_{\theta}^{(t)} is the index set of the top \lceil \tau K \rceil highest
16:
            values in S_{\theta}^{(t)};
            if \Psi^{(t+1)} \stackrel{\sigma}{<} \epsilon then
17:
                 break:
18.
19:
            end if
20: end for
21: return (\hat{\theta}_0, \hat{r}_0) = (\mathbb{E}[\Psi_{\theta}^{(t+1)}], \mathbb{E}[\Psi_r^{(t+1)}])
```

4 LoS-prior-enhanced CE scheme

In the THz near-field channel, it is noted that the LoS path is dominant and accounts for the majority of the received energy, which may mask the weak NLoS components in the noise [34]. By exploiting the estimated LoS information in Section 3, in this section, we propose a LoS-prior-enhanced CE (LPE-CE) scheme, which strategically decouples the LoS and NLoS components through subspace-orthogonal analog combiners, and then estimates the channel components separately to avoid NLoS components being masked. Additionally, we propose a lightweight near-field polar domain sparse codebook based on the LoS prior to reduce the computation complexity.

4.1 Subspace-orthogonal analog combiner design

Given the estimated LoS parameters $(\hat{\theta}_0, \hat{r}_0)$ in Section 3, we can easily obtain the steering vector of LoS path $\mathbf{b}(\hat{\theta}_0, \hat{r}_0)$ in (4). The normalized LoS direction vector is therefore given by

$$\mathbf{u}_0 = \frac{\mathbf{b}\left(\hat{\theta}_0, \hat{r}_0\right)}{\left\|\mathbf{b}\left(\hat{\theta}_0, \hat{r}_0\right)\right\|} = \mathbf{b}\left(\hat{\theta}_0, \hat{r}_0\right). \tag{18}$$

Motivated by the LoS dominance in THz channels, we align one of the combiner vectors directly with \mathbf{u}_0 to maximize the gain along this path, thereby capturing the bulk of the LoS energy. For the remaining vectors, we aim to span the spatial dimensions beyond the LoS direction to focus on NLoS components, while minimizing LoS interference. Specifically, we propose the following design strategy that enforces orthogonality between these additional combiner vectors and the LoS direction.

Firstly, for each combiner matrix $V_{A,q}$ $(q = Q_1 + 1, ..., Q_1 + Q_2)$, the first column is set as the LoS direction

$$\mathbf{v}_{A,a,1} = \mathbf{u}_0. \tag{19}$$

This alignment maximizes the received signal strength for the LoS component in the corresponding RF chain

Then, for the remaining combiner vectors $\mathbf{v}_{A,q,2}, \dots, \mathbf{v}_{A,q,M}$, we impose the orthogonality condition by the Gram-Schmidt orthogonalization process [35]

$$\mathbf{v}_{A,q,m}^{\mathrm{H}}\mathbf{u}_{0}=0, \quad m=2,\ldots,M. \tag{20}$$

Gram-Schmidt orthogonalization is employed here for its simplicity and ability to generate an orthonormal basis starting from random or predefined vectors, iteratively subtracting projections onto previous vectors. This orthogonality ensures that these vectors do not capture signals along the LoS direction, thereby focusing on the extraction of NLoS components. For ease of description, let $\mathbf{u}_{m-1} = \mathbf{v}_{A,q,m}$ ($m = 1, \ldots, M$). Consequently, the full combiner matrix can be written as $\mathbf{V}_{A,q} = \mathbf{U} = [\mathbf{u}_0, \ldots, \mathbf{u}_{M-1}]$.

This design creates a subspace-orthogonal combiner matrix **U** that projects the received signal into decoupled dimensions, enabling the separation of LoS and NLoS components across different RF chains, and thereby facilitating the subsequent CE. With the combiner matrix **U** designed, the next step is to construct an adaptive polar-domain codebook leveraging the LoS prior, which will be used for NLoS component estimation.

4.2 LoS-prior-aided adaptive polar-domain codebook

The THz near-field channel exhibits inherent sparsity in the polar domain, where the multipath components are sparsely distributed across a limited number of angle-distance pairs (θ_l, r_l) . This sparsity allows the channel to be efficiently represented using the polar-domain dictionary, facilitating CS-based reconstruction with low computational overhead [23]. Based on the estimated LoS parameters from Section 3, we propose an adaptive polar-domain codebook Ψ to exploit the channel sparsity.

As the channel characteristics depend on both angle and distance parameters in the near field, the conventional polar-domain codebook [23] consists of near-field steering vectors $\mathbf{b}(\theta, r)$ corresponding to a grid of angles θ and distances r. Typically, the entire polar domain is divided into S distance rings r_1, \ldots, r_S , while each distance ring is segmented by N uniform angle samples, yielding a total codebook size of $N \times NS$. For the n-th samples angle, the sampled distance of the s-th distance ring

 $r_{n,s} = Z\Delta(1-\bar{\theta}_n^2)/s$, where $Z_\Delta = \frac{N^2d^2}{2\beta_\Delta^2\lambda}$ is the threshold distance defined to limit the column coherence between two near-field steering vectors, β is the column coherence threshold. This approach requires sampling all possible angle-distance combinations, leading to a surge in sample count and computational complexity.

To address the challenge, we exploit the LoS parameters estimated in Section 3 to initialize a minimal codebook. As the diffraction and scattering are limited in THz channels, NLoS paths are dominated by nearby surfaces or objects along or close to the LoS path, rather than distant or highly deviated paths [27]. Therefore, we exploit the LoS parameters as the basis to generate the initial codebook, and the generation proceeds as follows.

(1) Initial distance ring computation. Given the desired column coherence threshold β_{Δ} , we have $Z_{\Delta} = \frac{N^2 d^2}{2\beta_{\Delta}^2 \lambda}$. Then, the minimum number of distance rings containing LoS path can be calculated as

$$s_0 = \left| \frac{Z_\Delta \left(1 - \hat{\theta}_0^2 \right)}{\hat{r}_0} \right|, \tag{21}$$

where s_0 is a positive integer. To provide initial coverage, we take $\bar{s}_0 = s_0 - 1$ as the upper bound of the distance ring sampling.

(2) Initial codebook generation. For each uniformly sampled angle $\bar{\theta}_n = n - \frac{N-1}{2}, n = 1, \dots, N$, calculate the corresponding s-th distance ring

$$\bar{r}_{n,s} = \frac{Z_{\Delta} \left(1 - \bar{\theta}_n^2\right)}{s}, \quad s = \bar{s}_0, \dots, \bar{s}_0 + \bar{S} - 1,$$
 (22)

where \bar{S} is the total number of distance rings that satisfies $\bar{S} + \bar{s}_0 = \left\lfloor \frac{Z_{\Delta}}{r_{\min}} \right\rfloor = S$. Therefore, the initial codebook can be generated as

$$\Psi_{\text{Init}} = [\Psi_1, \dots, \Psi_{\bar{S}}], \tag{23}$$

where $\Psi_s = \left[\mathbf{b} \left(\bar{\theta}_1, \bar{r}_{s,1} \right), \dots, \mathbf{b} \left(\bar{\theta}_N, \bar{r}_{s,N} \right) \right].$

In this way, the total size of the generated codebook reduces to $N \times N\bar{S}$. The codebook size shrink ratio is

$$\frac{\bar{S}}{S} = 1 - \frac{\bar{s}_0}{S} = 1 - \left| \frac{Z_\Delta (1 - \hat{\theta}_0^2)}{\hat{r}_0} \right| / \left[\frac{Z_\Delta}{r_{\min}} \right]. \tag{24}$$

Given that $\hat{\theta}_0$ is bounded within (-1,1), the limits of the aforementioned equation are derived as

$$1 - \left| \frac{Z_{\Delta}}{\hat{r}_0} \right| / \left| \frac{Z_{\Delta}}{r_{\min}} \right| \leqslant \frac{\bar{S}}{S} < 1.$$
 (25)

The inequality holds since $\hat{r}_0 > r_{\min}$. This compact initial codebook exploits the LoS prior to focus on likely NLoS path locations, reducing computational overhead. The codebook will be adaptively expanded during the NLoS estimation process, as described in Subsection 4.3.

4.3 Hierarchical decoupled estimation of LoS and NLoS components

With the subspace-orthogonal combiner U and the initial polar-domain codebook $\Psi_{\rm init}$, we now estimate the LoS and NLoS components separately from the combiner outputs. The motivation here is to exploit the orthogonal projection to isolate the dominant LoS signal first, then recover the residual NLoS paths. Specifically, the proposed hierarchical approach leverages the LoS prior for efficient LoS estimation and the polar-domain sparsity [23] of THz near-field channels for NLoS recovery via CS.

According to (1), the analog received signal after applying U is given by

$$\mathbf{y}_q = \mathbf{U}^{\mathrm{H}} \mathbf{h} s_q + \mathbf{U}^{\mathrm{H}} \mathbf{w}_q. \tag{26}$$

Stacking the signals across all Q_2 $(q=Q_1+1,\ldots,Q_1+Q_2)$ slots, the whole analog received signal $\mathbf{Y}=[\mathbf{y}_{Q_1+1},\ldots,\mathbf{y}_{Q_1+Q_2}]\in\mathbb{C}^{M\times Q_2}$ thereby is

$$Y = U^{H}hs + U^{H}W = h_{eff}s + U^{H}W,$$
(27)

where we assuming $\mathbf{s} = [1, \dots, 1]^{\mathrm{T}} \in \mathbb{C}^{1 \times Q_2}$. $\mathbf{W} = [\mathbf{w}_{Q_1+1}, \dots, \mathbf{w}_{Q_1+Q_2}] \in \mathbb{C}^{N \times Q_2}$ is the stacked noise matrix. Define $\mathbf{h}_{\mathrm{eff}} = \mathbf{U}^{\mathrm{H}} \mathbf{h} \in \mathbb{C}^{M \times 1}$ as the effective low-dimensional channel after projection. It can be estimated by the least squares (LS) method

$$\hat{\mathbf{h}}_{\text{eff}} = \mathbf{Y} \left(\mathbf{s}^{\text{T}} \mathbf{s} \right)^{-1} \mathbf{s}^{\text{T}} = \frac{1}{Q_2} \mathbf{Y} \mathbf{s}^{\text{T}}.$$
 (28)

LS is chosen here due to its simplicity and optimality under Gaussian noise assumptions. With $\hat{\mathbf{h}}_{\text{eff}}$, the hierarchical CE proceeds in two stages.

(1) Stage 1: LoS component estimation. As the first column of U is the normalized LoS direction vector \mathbf{u}_0 , the first element of \mathbf{h}_{eff} primarily captures the LoS gain, which can be extracted as

$$\mathbf{h}_{\text{eff},1} = \mathbf{u}_0^{\text{H}} \mathbf{h} = \mathbf{u}_0^{\text{H}} \mathbf{h}_{\text{LoS}} + \mathbf{u}_0^{\text{H}} \mathbf{h}_{\text{NLoS}} = \alpha_0 + \mathbf{u}_0^{\text{H}} \sum_{l=1}^{L} \alpha_l \mathbf{b}(\theta_l, r_l). \tag{29}$$

Given the LoS prior $\mathbf{u}_0 \approx \mathbf{b}(\theta_0, r_0)$ and the approximate orthogonality of near-field steering vectors, the inner product $\mathbf{u}_0^H \mathbf{b}(\theta_l, r_l) \approx 0$ for $l \neq 0$. This orthogonality assumption holds well in THz regimes with large arrays, as paths are sparsely distributed [29]. Thus, the residual NLoS term is negligible, allowing direct estimation of the LoS complex gain

$$\hat{\alpha}_0 = \hat{\mathbf{h}}_{\text{eff},1},\tag{30}$$

and reconstruction of the LoS channel

$$\hat{\mathbf{h}}_{\text{LoS}} = \hat{\alpha}_0 \mathbf{u}_0. \tag{31}$$

This stage isolates the dominant path without iterative optimization.

(2) Stage 2: NLoS component estimation. After subtracting the estimated LoS from the effective channel, we obtain the NLoS residual in Q_2 slots

$$\mathbf{y}_{\mathrm{NLoS}} = \hat{\mathbf{h}}_{\mathrm{eff}} - \mathbf{U}^{\mathrm{H}} \hat{\mathbf{h}}_{\mathrm{LoS}}.$$
 (32)

Leveraging the polar-domain sparsity of the THz near-field channel, in this stage, we apply the CS approach to perform the NLoS CE. Let Ψ be the polar-domain codebook which is designed in Subsection 4.2 to match the near field sparsity and reduce size via LoS prior, the sparse reconstruction problem can be formulated as

$$\min_{\tilde{\mathbf{h}}} \|\tilde{\mathbf{h}}\|_{0}, \quad \text{s.t. } \|\mathbf{U}^{H}\mathbf{\Psi}\tilde{\mathbf{h}} - \mathbf{y}_{NLoS}\|_{2} \leqslant \kappa, \tag{33}$$

where $\tilde{\mathbf{h}}$ is the sparse support vector to be estimated, κ is the maximum tolerable error bound.

To solve this sparse reconstruction problem efficiently and robustly, we use an iterative orthogonal matching pursuit (OMP) algorithm [36] with adaptive codebook expansion. After each OMP iteration, we compute the residual norm $\|\mathbf{r}\|_2 = \|\mathbf{U}^H\mathbf{\Psi}\hat{\mathbf{h}} - \mathbf{Y}_{\text{NLoS}}\|_2$. If $\|\mathbf{r}\|_2 > \nu$, where ν is the residual threshold, we expand $\mathbf{\Psi}$ by adding a new distance ring (e.g., $s_{\text{new}} = \min(s) - 1$), computing new distances $\bar{r}_{n,s_{\text{new}}} = \frac{Z_{\Delta}(1-\bar{\theta}_n^2)}{s_{\text{new}}}$ for $n=1,\ldots,N$, and appending $\mathbf{\Psi}_{s_{\text{new}}} = [\mathbf{b}(\bar{\theta}_1,\bar{r}_{s_{\text{new}},1}),\ldots,\mathbf{b}(\bar{\theta}_N,\bar{r}_{s_{\text{new}},N})]$ to $\mathbf{\Psi}$. The OMP is re-run with warm-start, using the previous support set to reduce complexity. This repeats until $\|\mathbf{r}\|_2 \leqslant \nu$ or a maximum expansion limit E_{max} is reached. The NLoS channel is finally reconstructed as

$$\hat{\mathbf{h}}_{\mathrm{NLoS}} = \Psi \hat{\tilde{\mathbf{h}}}.\tag{34}$$

The complete channel estimation is obtained by combining the LoS and NLoS estimates

$$\hat{\mathbf{h}} = \hat{\mathbf{h}}_{LoS} + \hat{\mathbf{h}}_{NLoS}.\tag{35}$$

This adaptive mechanism ensures a compact codebook while covering sufficient paths, balancing accuracy and complexity.

4.4 Proposed LPE-CE algorithm

The overall LPE-CE procedure is summarized in Algorithm 2.

Algorithm 2 Proposed LPE-CE algorithm.

 $\textbf{Input:} \ \, \text{Estimated localization} \ (\hat{\theta}_0, \hat{r}_0), \ \text{received signal} \ \{\mathbf{y}_q\}_{q=Q_1+1}^{Q_1+Q_2}, \ \text{threshold} \ \beta_{\Delta}, \ \text{minimum allowable distance} \ r_{\min}, \ \text{number of localization} \}$ NLoS paths L, residual threshold ν , max expansions E_{max} . Output: Estimated channel $\hat{\mathbf{h}}$. 1: Initialization of LoS-prior-aided adaptive polar-domain codebook: 2: $Z_{\Delta} = \frac{N^2 d^2}{2\beta_{\Delta}^2 \lambda}$, $s_0 = \left[\frac{Z_{\Delta}(1 - \hat{\theta}_0^2)}{\hat{r}_0} \right]$, $\Psi = []$; 3: for $s = s_0 - 1$ to $s_0 + \bar{S}$ do 4: for $n \in \{1, \ldots, N\}$ do $\bar{\theta}_n = n - \frac{N-1}{2}, \bar{r}_{n,s} = \frac{Z_{\Delta}(1 - \bar{\theta}_n^2)}{s};$ Append $\mathbf{b}(\bar{\theta}_n, \bar{r}_{n,s})$ to Ψ_s ; 6: 7. end for 8: $\Psi = [\Psi, \Psi_s];$ 9: end for 10: Decoupled estimation of LoS and NLoS components: 11: Generate $\mathbf{U} = [\mathbf{u}_0, \dots, \mathbf{u}_{M-1}]$ in (19) and (20); 12: for $q = Q_1 + 1, \dots, Q_1 + Q_2$ do 13: Apply $V_{A,q} = U$ to acquire y_q in (26); 14: end for 15: Stacking all Q_2 slots to acquire **Y** in (27); 16: Estimate the effective channel $\hat{\mathbf{h}}_{\text{eff}}$ in (28); 17: Stage 1: LoS component 18: $\hat{\alpha}_0 = \hat{\mathbf{h}}_{\text{eff},1}, \hat{\mathbf{h}}_{\text{LoS}} = \hat{\alpha}_0 \mathbf{u}_0;$ 19: Stage 2: Adaptive NLoS component 20: Residual signal $\mathbf{Y}_{\text{NLoS}} = \hat{\mathbf{h}}_{\text{eff}} - \mathbf{U}^{\text{H}} \hat{\mathbf{h}}_{\text{LoS}};$ 21: Expansion counter and previous support: e = 0, supp_{prev} = {}; 22: while $e < E_{\rm max}$ do $\label{eq:normalization: r = y_NLoS} Initialization: \ \mathbf{r} = \mathbf{y}_{\mathrm{NLoS}}, \bar{\boldsymbol{\Psi}} = \mathbf{U}^{\mathrm{H}}\boldsymbol{\Psi}, \mathrm{supp} = \mathrm{supp}_{\mathrm{prev}};$ 23: 24: for $l \in \{1, ..., L\}$ do Calculate the correlation matrix: $\Gamma = \bar{\Psi}^{H}\mathbf{R}$; 25: $\label{eq:update support set: supp} \text{Update support set: supp} = \text{supp} \cup \{\arg\max_i \bar{\boldsymbol{\Psi}}_i^{\text{H}} \mathbf{R}\};$ 26: $\mathrm{LS:}\ \hat{\tilde{\mathbf{h}}} = (\boldsymbol{\Psi}_{\mathrm{supp}}^{\mathrm{H}} \boldsymbol{\Psi}_{\mathrm{supp}})^{-1} \boldsymbol{\Psi}_{\mathrm{supp}}^{\mathrm{H}} \mathbf{y}_{\mathrm{NLoS}};$ 27: Update residual $\mathbf{r} = \mathbf{r} - \mathbf{\Psi}_{\text{supp}} \tilde{\mathbf{h}};$ 28: 29: end for if $\|\mathbf{r}\|_2 \leqslant \epsilon$ then 30: 31: break 32: else 33: Add outward ring: $s_{\text{new}} = \min(s) - 1$; 34: for $n \in \{1, \dots, N\}$ do $\bar{r}_{n,s_{\text{new}}} = \frac{Z_{\Delta}(1-\bar{\theta}_n^2)}{s_{\text{new}}};$ 35: Append $\mathbf{b}(\bar{\theta}_n, \bar{r}_{n,s_{\text{new}}})$ to $\Psi_{s_{\text{new}}}$; 36: 37: end for $oldsymbol{\Psi} = [oldsymbol{\Psi}, oldsymbol{\Psi}_{s_{ ext{new}}}];$ 38: 39. Warm-start next OMP: $supp_{prev} = supp;$ 40: 41: end if

5 Simulation results

44: return $\hat{\mathbf{h}} = \hat{\mathbf{h}}_{LoS} + \hat{\mathbf{h}}_{NLoS}$.

42: end while 43: $\hat{\mathbf{h}}_{NLoS} = \Psi \hat{\tilde{\mathbf{h}}};$

In this section, we evaluate the localization and CE performance based on the proposed methods via numerical simulations.

5.1 Simulation setup

Through the simulation, we consider a hybrid analog and digital UM-MIMO system with N=256-antenna ULA and M=8 RF chains at carrier frequency f=100 GHz. The spatial angles of the user and L=2 scatterers to the center of BS are set as $\theta \sim \mathcal{U}(-1,1)$. The distance of the user to the center of BS is set to $r_0 \sim \mathcal{U}(2,10)$ m within the near-field region $D_{\text{Rayl}} = \frac{2N^2d^2}{\lambda} \approx 98$ m, and the distances of the scatterers are $r_l \sim \mathcal{U}(2,r_0+\Delta r)$, where $\Delta r=2$ m. The Rician K-factor k is set to 10 dB.

The performance of the localization algorithms is measured by the root of mean squared error (RMSE) for both angle and distance parameters, which is defined as RMSE = $\sqrt{\frac{1}{D}\sum_{i=1}^{D}|\hat{x}_i-x_0|^2}$, where $D=10^3$ is the Monte Carlo trials, and \hat{x}_i denotes the estimates of x at the i-th trial. Here x can be either the angle θ or the distance r. And the performances of CE algorithms are evaluated based on the normalized

Table 1 Details of localization algorithms.

Algorithm	Computational complexity (multiplications)	Average runtime (s)	
Proposed	$N^2 + t_{\max} MIKN$	0.0122	
CMR [18]	$N^{5} + N^{4} + N^{3} + \frac{\pi(r_{\text{max}} - r_{\text{min}})}{\delta^{2}} N^{2}$	41.8310	
SNRO [19]	$\frac{N^3}{M^2} + \frac{\pi(r_{\max} - r_{\min})}{\delta^2} MIN$	0.2016	
DE [22]	$N^2 + \frac{(r_{\text{max}} - r_{\text{min}})}{\delta} MIN$	0.0228	

mean square error (NMSE), which is defined as NMSE = $\frac{1}{D} \sum_{i=1}^{D} \|\hat{\mathbf{h}}_i - \mathbf{h}\|_2^2 / \|\mathbf{h}\|_2^2$, where $\hat{\mathbf{h}}_i$ denotes the estimates of $\hat{\mathbf{h}}$ at the *i*-th trial.

5.2 Localization performance

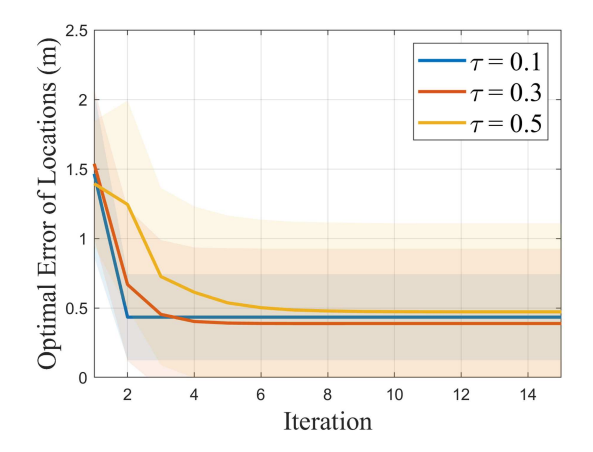
In this subsection, we compare the performance of the proposed localization algorithm with the following three baseline algorithms.

- Covariance matrix reconstruction (CMR) algorithm [18]. Reconstruct the spatial covariance matrix and then estimate both angle and distance from the spatial covariance matrix by 2-D MUSIC [37].
- SNR-optimal (SNRO) algorithm [19]. Both angle and distance are simultaneously exhaustively searched to maximize the output SNR.
- Decoupled estimation (DE) algorithm [22]. Since the angle estimation component utilizes the subarray of the partially connected architecture that cannot be extended to the fully connected architecture in this paper, we leverage the decoupling estimation concept of this approach. In the first step, angle estimation employs the coarse angle estimation scheme proposed in this paper; in the second step, distance estimation follows the original scheme.

The estimated range of all the algorithms is set to $(r_{\min}, r_{\max}) = (2, 15)$ m. The search resolution of both angle and distance in CMR and SNRO algorithms, and of distance in DE algorithm, is set to $\delta = 10^{-3}$. For the proposed algorithm, it is set that the predefined threshold $\bar{\eta} = 0.8$ [27], tolerance error $\epsilon = 10^{-3}$, sampling number K = 20, and interval shrinkage ratio $\tau = 0.3$. The pilot length of the sensing phase is $Q_1 = N/M$.

The computational complexity and average runtimes of the proposed algorithm and three baseline algorithms are listed in Table 1. The CMR algorithm incurs additional overhead due to the repeated matrix pseudo-inversions. The primary reason for the complexity gap between the proposed algorithm and the baselines (exhaustive search over both angles and distances in SNRO, and distance search in DE) lies in their brute-force optimization strategies. The computational complexity and average runtime advantages further demonstrate the superiority of our proposed alternating optimization approach. Additionally, Figure 4 illustrates the curve of the optimal error of the locations $\hat{l}_{\rm loc} = (\hat{\theta}_0, \hat{r}_0)$ in each iteration t of the proposed algorithm, with the interval shrinkage ratio $\tau \in \{0.1, 0.3, 0.5\}$. It can be observed from the figure that the convergence iteration $t_{\rm max}$ increases with τ , while the optimal estimation performance is achieved at $\tau = 0.3$, which can be attributed to the following trade-off. On the one hand, small τ values induce precocious convergence, causing the algorithm to terminate at suboptimal solutions (local optima) due to insufficient exploration. On the other hand, large τ values significantly reduce convergence speed while simultaneously increasing estimation variance, resulting from excessive exploration at the expense of exploitation efficiency.

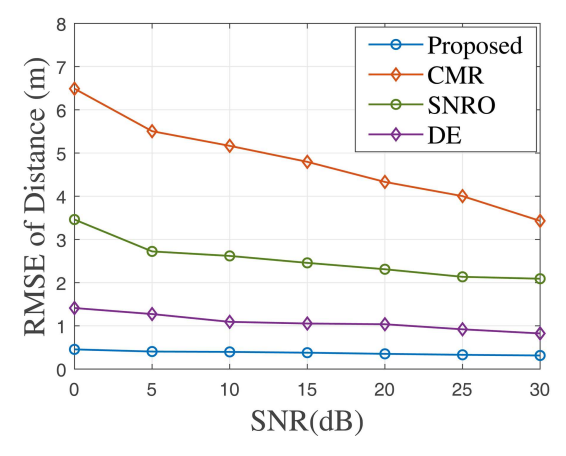
Figures 5 and 6 plot the curves of RMSE of spatial angle and distance versus SNR of the proposed algorithm and three baseline algorithms, respectively. From the two figures, it is obvious that as the SNR increases, the accuracy of the algorithms improves accordingly. The proposed localization scheme significantly outperforms the baseline algorithms at all considered SNR in both angle and distance estimation. For the angle estimation, due to the designed analog combiner matrix that performs pre-judgment on the signal's spatial sector, the proposed, SNRO and DE algorithms all achieve superior angle estimation performance. Particularly, the superior angle estimation performance of DE algorithm effectively validates the efficiency of the coarse angle estimation scheme presented in Subsection 3.1. For the distance estimation, both far-field algorithms (CMR and SNRO) exhibit significant estimation errors, which reveal the limitations of directly extending one-dimensional far-field search schemes to two-dimensional near-field search. The one-dimensional search after decoupling angle and distance enables DE algorithm to achieve superior distance estimation performance compared to far-field schemes. However, constrained by the limited accuracy of coarse angle estimation, residual errors in distance estimation remain unavoidable. Therefore, the effectiveness of the proposed scheme for near-field localization is rigorously verified.



0.25 Proposed RMSE of Spatial Angle **CMR** 0.2 -SNRO DE 0.15 0.1 0.05 0 0 10 15 20 SNR(dB)

Figure 4 (Color online) The optimal error of the locations in each iteration of the proposed algorithm, with different interval shrinkage ratios (the solid line is the mean of the error, and the blocks in the corresponding color are the error bands (mean \pm standard deviation)), where SNR = 10 dB.

Figure 5 (Color online) RMSE of spatial angle versus SNR.



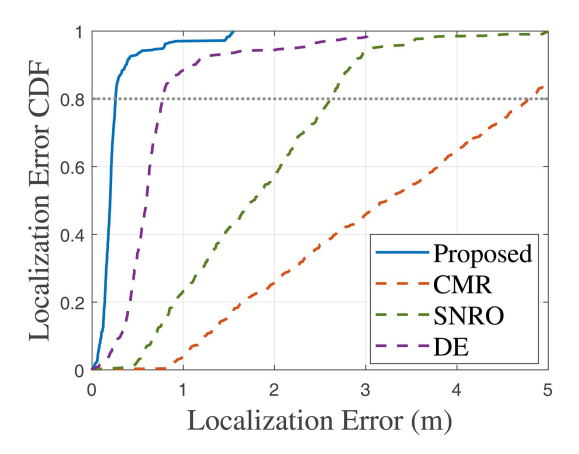


Figure 6 (Color online) RMSE of distance versus SNR.

Figure 7 (Color online) The CDF of localization error.

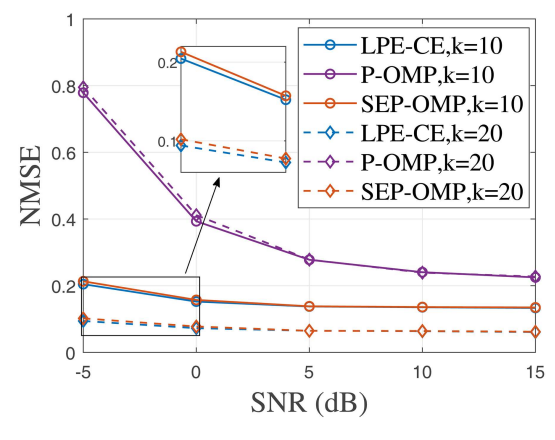
Figure 7 demonstrates the cumulative distribution functions (CDFs) of localization errors for the proposed and three baseline algorithms at SNR = 10 dB. It can be seen that the proposed algorithm achieves rapid CDF growth in low-error regimes, attaining 80% localization accuracy within 0.3 m, and 95% success rate at 1-m error. Although all algorithms show CDF improvement with increasing error tolerance, the proposed algorithm maintains consistent dominance, reaching full convergence within 1.5 m. These results validate the proposed scheme's capability to deliver localization reliability essential for 6G ultra-reliable low-latency applications.

5.3 CE performance

In this subsection, we compare the performance of the proposed CE algorithm with the following two baseline algorithms.

- Conventional polar-domain OMP (P-OMP) algorithm. The CE process strictly follows [23] without any LoS prior, and thus does not involve LoS/NLoS decoupling.
- Separate estimation by conventional polar-domain codebook (SEP-OMP). Initial LoS component estimation is performed according to the presented scheme, after which the resulting NLoS residual signal undergoes estimation using the conventional polar-domain codebook.

The angle grids of the codebook of all the algorithms are uniformly selected within (-1,1) as $\bar{\theta}_n = n - \frac{N-1}{2}$ for n = 1..., N. The codebook desired column coherence threshold is set to $\beta_{\Delta} = 0.8$ [23,38]. The pilot length Q_2 is set to 50 and the expansion residual threshold in the proposed $\nu = 0.1\sigma\sqrt{M}$.



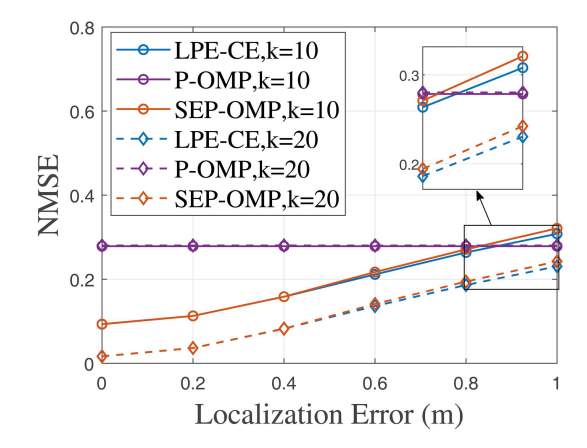
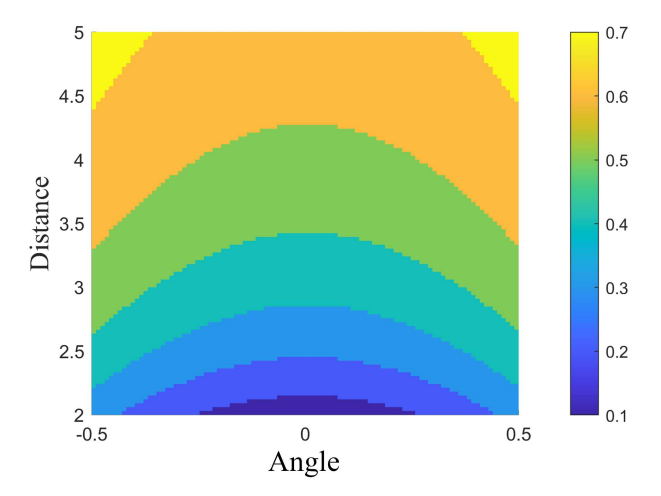


Figure 8 (Color online) NMSE versus SNR with K-factor $k=10,20\,$ dB, respectively.

Figure 9 (Color online) NMSE versus localization error with K-factor k = 10, 20 dB, respectively.



 ${\bf Figure~10~~(Color~online)~Initial~codebook~size~shrink~ratio~versus~angle~and~distance.}$

Figure 8 provides the NMSE performance of CE versus SNR with K-factor k=10,20 dB, respectively, where the localization errors are set to 0.3 m. It can be observed from the figure that across -5 to 15 dB SNR, all methods exhibit a monotonic NMSE decrease. LPE-CE slightly outperforms SEP-OMP, especially in low SNR, indicating the better noise robustness of the proposed adaptive codebook. Both of them consistently outperform P-OMP, confirming that first estimating and canceling the LoS component alleviates masking of weaker NLoS paths. When the K-factor increases from 10 to 20 dB, P-OMP gains a slight degradation due to stronger masking, while LPE-CE and SEP-OMP get an increase because they explicitly decouple LoS and NLoS.

Figure 9 compares the NMSE performance of CE versus the localization errors with K-factor k=10,20 dB, respectively, where the SNR is set to 5 dB. As the localization error grows from 0 to 1 m, NMSE increases for both LPE-CE and SEP-OMP, while it remains constant for P-OMP as it does not exploit localization prior. LPE-CE degrades more slowly than SEP-OMP, owing to a polar-domain sparse codebook searched under a residual-threshold rule that adaptively expands the distance ring only when needed, compensating for biases in the localization prior and yielding higher robustness to localization errors.

Additionally, to validate the lightweight degree of the proposed LoS-prior-aided codebook, we plot the codebook size shrink ratio function $\frac{\bar{S}}{S}$ in (24) versus different angles and distances, as illustrated in Figure 10. It can be seen in the figure that the codebook size shrink ratio demonstrates an overall decreasing trend with the reducing distance \hat{r}_0 . When \hat{r}_0 approaches r_{\min} , the codebook shrink ratio reaches 0.1, indicating an order-of-magnitude reduction in codebook size. And the shrink ratio predominantly remains within the 0.3–0.7 range. Moreover, the average number of codebook expansions is 0.02 across all trials. Hence, the final codebook size is nearly identical to the initial one, preserving the order-of-

magnitude reduction over the full codebook. For UM-MIMO systems featuring hundreds to thousands of antenna elements, the proposed LoS-prior codebook effectively reduces the codebook size, which may achieve significant computational complexity reduction.

6 Conclusion

In this paper, we propose a joint localization and CE scheme in THz near-field UM-MIMO ISAC systems. The proposed scheme achieves precise localization via coarse AoA estimation and refined optimization, while the LPE-CE scheme boosts channel estimation accuracy with an adaptive codebook that dynamically expands based on residuals. By reducing system complexity and hardware needs, it supports practical 6G ISAC deployment. Future work could extend this approach to dynamic environments.

Acknowledgements This work was supported by Beijing Natural Science Foundation (Grant No. L223007).

References

- 1 Chowdhury M Z, Shahjalal M, Ahmed S, et al. 6G wireless communication systems: applications, requirements, technologies, challenges, and research directions. IEEE Open J Commun Soc, 2020, 1: 957–975
- 2 Liu F, Cui Y, Masouros C, et al. Integrated sensing and communications: toward dual-functional wireless networks for 6G and beyond. IEEE J Sel Areas Commun, 2022, 40: 1728–1767
- 3 Wei Z, Qu H, Wang Y, et al. Integrated sensing and communication signals toward 5G-A and 6G: a survey. IEEE Int Things J, 2023, 10: 11068-11092
- 4 Chen H, Sarieddeen H, Ballal T, et al. A tutorial on terahertz-band localization for 6G communication systems. IEEE Commun Surv Tut, 2022, 24: 1780–1815
- 5 Ma Z T, Geng Z X, Fan Z Y, et al. Modulators for terahertz communication: the current state of the art. Research, 2019, 2019: 2019/6482975
- 6 Wang Z, Zhang J, Du H, et al. A tutorial on extremely large-scale MIMO for 6G: fundamentals, signal processing, and applications. IEEE Commun Surv Tut, 2024, 26: 1560–1605
- 7 Liu Z, Yang C, Peng M. Integrated sensing and communications in terahertz systems: a theoretical perspective. IEEE Netw, 2023, 38: 194–201
- 8 Wang Y, Yang C, Ren Z, et al. Sensing-aided hybrid precoding for efficient terahertz wideband communications in multiuser high-data-rate IoT. IEEE Int Things J, 2023, 11: 8253-8267
- 9 Fan Y, Yang C, Sun Y, et al. Hybrid channel tracking for THz massive MIMO communication systems in dynamic environments. IEEE J Sel Areas Commun, 2025, 43: 988–1003
- Huang Z, Wang K, Liu A, et al. Joint pilot optimization, target detection and channel estimation for integrated sensing and communication systems. IEEE Trans Wireless Commun, 2022, 21: 10351–10365
- 11 Chen X, Feng Z, Zhang J A, et al. Sensing-aided uplink channel estimation for joint communication and sensing. IEEE Wireless Commun Lett, 2023, 12: 441–445
- 12 Mundlamuri R, Gangula R, Thomas C K, et al. Sensing aided channel estimation in wideband millimeter-wave MIMO systems. In: Proceedings of IEEE International Conference on Communications Workshops (ICC Workshops), 2023. 1404–1409
- 13 Ren Z, Qiu L, Xu J, et al. Sensing-assisted sparse channel recovery for massive antenna systems. IEEE Trans Veh Technol, 2024, 73: 17824–17829
- 14 Ning B, Tian Z, Mei W, et al. Beamforming technologies for ultra-massive MIMO in terahertz communications. IEEE Open J Commun Soc, 2023, 4: 614–658
- 15 Gao X, Dai L, Sayeed A M. Low RF-complexity technologies to enable millimeter-wave MIMO with large antenna array for 5G wireless communications. IEEE Commun Mag, 2018, 56: 211–217
- 16 Sohrabi F, Yu W. Hybrid analog and digital beamforming for mmWave OFDM large-scale antenna arrays. IEEE J Sel Areas Commun. 2017. 35: 1432–1443
- 17 Zhang R, Shim B, Wu W. Direction-of-arrival estimation for large antenna arrays with hybrid analog and digital architectures. IEEE Trans Signal Process, 2021, 70: 72–88
- 18 Liu Y, Yan Y, You L, et al. Spatial covariance matrix reconstruction for DOA estimation in hybrid massive MIMO systems with multiple radio frequency chains. IEEE Trans Veh Technol, 2021, 70: 12185–12190
- 19 Abdelbadie A, Mostafa M, Bameri S, et al. DoA estimation for hybrid receivers: full spatial coverage and successive refinement. IEEE Trans Signal Process, 2024, 72: 4730–4744
- 20 Rodriguez-Fernández J, González-Prelcic N, Venugopal K, et al. Frequency-domain compressive channel estimation for frequency-selective hybrid millimeter wave MIMO systems. IEEE Trans Wireless Commun, 2018, 17: 2946–2960
- 21 Cui M, Wu Z, Lu Y, et al. Near-field MIMO communications for 6G: fundamentals, challenges, potentials, and future directions. IEEE Commun Mag, 2022, 61: 40–46

- 22 Sun Y, Yang C, Peng M. Efficient near-field localization for hybrid analog and digital UM-MIMO systems. In: Proceedings of VTC Spring 2025-IEEE Vehicular Technology Conference, 2025
- 23 Cui M, Dai L. Channel estimation for extremely large-scale MIMO: far-field or near-field? IEEE Trans Commun, 2022, 70: 2663–2677
- 24 Yang S J, Peng Y Z, Lyu W T, et al. Near-field channel estimation for extremely large-scale terahertz communications. Sci China Inf Sci, 2024, 67: 192302
- 25 Liu S, Yu X, Gao Z, et al. Sensing-enhanced channel estimation for near-field XL-MIMO systems. IEEE J Sel Areas Commun, 2025, 43: 628-643
- 26 Xilinx A. Zynq UltraScale+ RFSoC RF data converter v2.6 gen 1/2/3/DFE. 2022. https://docs.amd.com/r/en-US/pg269-rf-data-converter
- 27 Moldovan A, Ruder M A, Akyildiz I F, et al. LOS and NLOS channel modeling for terahertz wireless communication with scattered rays. In: Proceedings of 2014 IEEE Globecom Workshops (GC Wkshps), 2014. 388–392
- 28 Xing Y, Rappaport T S. Propagation measurements and path loss models for sub-THz in urban microcells. In: Proceedings of ICC 2021-IEEE International Conference on Communications, 2021. 1–6
- 29 Elbir A M, Mishra K V, Chatzinotas S. Terahertz-band joint ultra-massive MIMO radar-communications: model-based and model-free hybrid beamforming. IEEE J Sel Top Signal Process, 2021, 15: 1468–1483
- 30 Sherman J. Properties of focused apertures in the Fresnel region. IRE Trans Antennas Propag, 1962, 10: 399-408
- 31 Sohrabi F, Yu W. Hybrid digital and analog beamforming design for large-scale antenna arrays. IEEE J Sel Top Signal Process, 2016, 10: 501–513
- 32 Zhang Y, Wu X, You C. Fast near-field beam training for extremely large-scale array. IEEE Wireless Commun Lett, 2022, 11: 2625–2629
- 33 Sherman J. Properties of focused apertures in the Fresnel region. IRE Trans Antennas Propag, 1962, 10: 399-408
- 34 Ghermezcheshmeh M, Zlatanov N. Parametric channel estimation for LoS dominated holographic massive MIMO systems. IEEE Access, 2023, 11: 44711–44724
- 35 Björck Å. Numerics of Gram-Schmidt orthogonalization. Linear Algebra its Appl, 1994, 198: 297-316
- 36 Lee J, Gil G T, Lee Y H. Channel estimation via orthogonal matching pursuit for hybrid MIMO systems in millimeter wave communications. IEEE Trans Commun, 2016, 64: 2370–2386
- 37 Huang Y D, Barkat M. Near-field multiple source localization by passive sensor array. IEEE Trans Antennas Propagat, 1991, 39: 968–975
- 38 Cui M Y, Dai L L. Near-field wideband channel estimation for extremely large-scale MIMO. Sci China Inf Sci, 2023, 66: 172303